

Observing the Sun from start to finish: The Tunable magnetograph's design, calibration, data reduction and scientific exploitation.

PhD dissertation by

Pablo Santamarina Guerrero

Instituto de Astrofísica de Andalucía (IAA-CSIC)

Programa de Doctorado en Física y Matemáticas (FisyMat)
Universidad de Granada

A thesis submitted in fulfillment
of the requirements of the degree of
Doctor of Philosophy

October 3, 2024

PhD thesis supervised by

Dr. David Orozco Suárez

Dr. Julián Blanco Rodríguez



INSTITUTO DE
ASTROFÍSICA DE
ANDALUCÍA



EXCELENCIA
SEVERO
OCHOA



UNIVERSIDAD
DE GRANADA

CONTENTS

1	Sunrise III and TuMag: Design and calibration.	1
1.1	Sunrise III	2
1.1.1	Observatory's design	3
1.1.2	Science with Sunrise.	4
1.2	The Tunable magnetograph: TuMag	6
1.3	TuMag's design and light path.	6
1.4	Instrument performance and verification.	8
1.4.1	Imaging performance.	9
1.4.2	Spectral performance.	12
1.4.3	Polarimetric performance.	15
2	TuMag's pipeline and data.	19
2.1	TuMag's observing modes	19
2.1.1	Calibration modes	20
2.1.1.1	Flat-field observations	21
2.1.1.2	Dark-current observations	22
2.1.1.3	Linear polarizer and micropolarizers observations.	23
2.1.1.4	Pinhole Observations.	23
2.1.1.5	Straylight target.	23
2.1.1.6	Prefilter scans.	24
2.1.1.7	Phase diversity.	24
2.2	Pipeline	24
2.2.1	Darks and flat fields	24
2.2.2	Blueshift	24
2.2.3	Demodulation and dual beam	24
2.2.4	Cross Talk	24

CHAPTER 1

SUNRISE III AND TUMAG: DESIGN AND CALIBRATION.

Observing the Sun with the highest possible quality and resolution is crucial for deepening our understanding of the physical processes governing its behavior. This necessity drives the continuous development of new state-of-the-art observatories and advanced instrumentation. Each new instrument or telescope builds upon the technical achievements of its predecessors, integrating past knowledge while introducing innovations that push the boundaries of solar observation.

An example of such advancements is the third edition of the Sunrise observatory, which marks the culmination of a collaborative effort among several international institutions. Spearheaded by the Max Planck Institute for Solar System Research (MPS) in Göttingen, Germany, the international consortium is also composed by the Spanish Solar Space Consortium (S³PC), the National Astronomical Observatory of Japan (NAOJ), the Kiepenheuer Institute for Solar Physics (KIS) in Freiburg, Germany, and the Johns Hopkins University Applied Physics Laboratory (APL) in the United States.

Following an initial unsuccessful flight in 2022, which was aborted six hours after launch, Sunrise III was granted a second opportunity in the summer of 2024. On July 10th, 2024, at 04:22:40 UTC, the observatory was successfully launched by the Columbia Scientific Balloon facility (CSBF-NASA) from Esrange, a scientific facility operated by the Swedish Space Corporation in Kiruna, Sweden. After reaching a stable altitude of 37.5 km, the commissioning phase began, marking the official start of the observation campaign. Observations commenced shortly thereafter and continued until the campaign concluded on July 16th at 18:20:54 UTC, when the flight was terminated.

Among the payload instruments aboard Sunrise III, TuMag holds particular significance for this thesis. TuMag, an imaging magnetograph developed by the Spanish Solar Space Consortium (S³PC) under the leadership of the Instituto de Astrofísica de Andalucía (IAA-CSIC) in Granada. The S³PC also includes the Instituto Nacional de Técnica Aeroespacial (INTA), the Instituto de la Riva (IDR-UPM) at the Universidad Politécnica de Madrid, the Universitat de València (UV), and the Instituto de Astrofísica de Canarias (IAC). TuMag is central to this thesis, as the core of the work focuses on its calibration, operations, and data reduction processes.

In this chapter, we present an overview of the Sunrise III mission, with a particular focus on the Tunable Magnetograph (TuMag). We will first outline the scientific motivations behind its development and the design choices. This will be followed by a detailed discussion of the technical specifications of both the mission and TuMag.

1.1 Sunrise III

Equipped with a telescope with a 1m aperture, two slit-based spectropolarimeters and an imaging magnetograph, the Sunrise III observatory is the most complex solar telescope to ever leave the ground. The coordination of three different scientific instruments allows Sunrise to simultaneously perform narrow-band polarimetric imaging in the visible while carrying out spectropolarimetry in the near-UV and near-IR, from the advantageous point of observation of ~ 36 km of altitude without the annoying interference of the atmosphere's turbulence.

The three instruments aboard Sunrise III have been carefully designed to complement each other and address the scientific purposes of the mission. The Tunable Magnetograph (TuMag, REF), developed by the S³PC, carries out high-spatial-resolution imaging spectropolarimetry in the visible range of light. Able to tune to three different spectral lines, namely the highly Zeeman-sensitive iron lines at 525.02 and 525.06 nm, and the Mg I b₂ line, TuMag can probe the photosphere and low chromosphere quasi-simultaneously.

The absence of atmosphere allows the Sunrise Spectropolarimeter and Imager (SUSI, Ref), developed by MPS and NAOJ, to observe in the near-UV, performing imaging and spectropolarimetry in the range of 309-417 nm. The high polarimetric sensitivity and large number of spectral lines present in this range, many of which are sensible to the Hanle effect, allows SUSI to sample many heights in the solar atmosphere at the same time while measuring the weak magnetic fields.

In the same way that the atmosphere complicates the observations of the UV range from the ground, observations of many lines in the near-IR are also unfeasible with ground-based instruments due to the telluric contamination of the atmosphere. The Sunrise Chromospheric Infrared spectro-Polarimeter (SCIP, REF), co-developed by NAOJ and IAA-CSIC, takes advantage of the absence of atmosphere and observes two of the Ca II triplets lines. Spectropolarimetry measurements of these lines provides information of the 3-D structure of the chromosphere and its magnetic fields, derived thanks to the high zeeman sensitivity of the selected lines. Furthermore, the large number of available photons at these wavelengths ensures a high S/N and polarimetric sensitivities.

The ability to probe simultaneously the near-IR, the visible and the near-UV, performing high-resolution polarimetric imaging and spectroscopy makes Sunrise III an unique observatory, capable of studying the connection and interaction of the small-scale phenomena occurring at different layers of the solar's atmosphere with unprecedented detail and completeness.

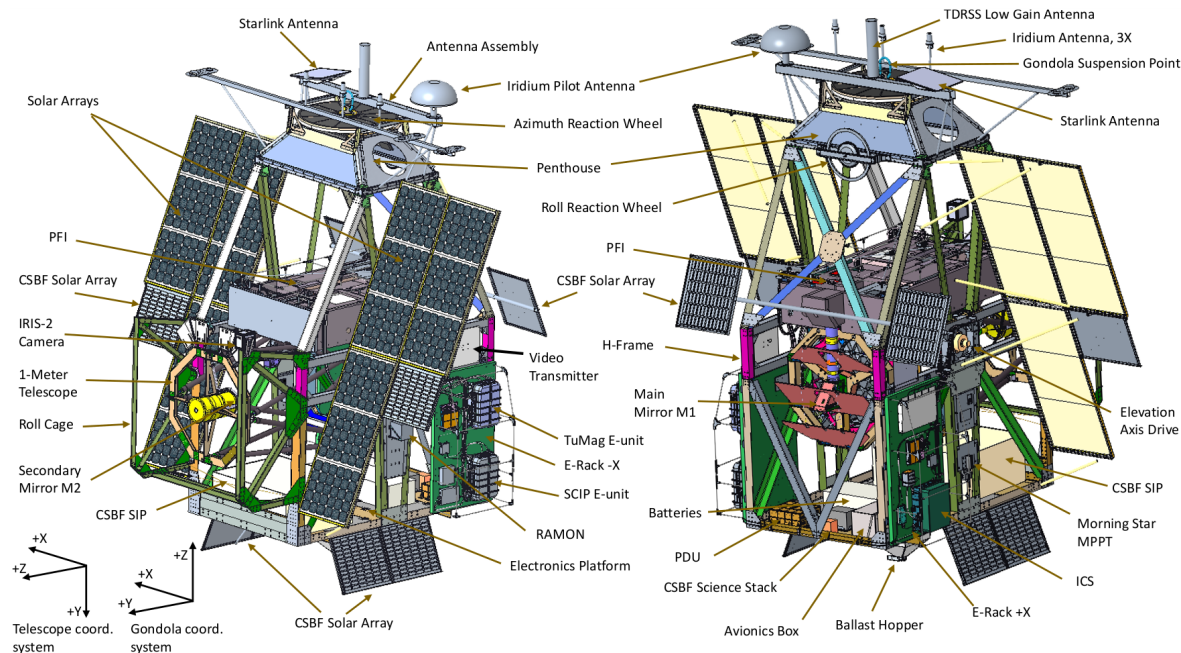


Figure 1.1 Drawing design of the Sunrise III observatory. Image reproduced from XXXXX with permission. **No he pedido permiso para esta aún, que es del paper de Sunrise III que mandó Andi, pero creo que quedaría bien algo enseñando el observatorio. Al no estar publicado el paper de Sunrise no se muy bien cual coger.**

1.1.1 Observatory's design

While the scientific instruments are central to the research performed by Sunrise, several additional subsystems play a crucial role, each contributing to the overall success of the mission.

The structural framework housing all components of the observatory, as well as the interface connecting the observatory to the flight apparatus, is provided by the gondola. This gondola, engineered by APL, is not only tasked with safeguarding the instruments and telescope during ascent and landing, but also with ensuring the stability of the pointing system. Given that the observatory is suspended from a balloon, it is subject to wind-induced motion and pendulum-like oscillations, which threaten the stability required for prolonged observations. The gondola's pointing control system (PCS) must actively counteract these disturbances in real time by making precise adjustments to the telescope's elevation and azimuth. In conjunction with the Correlating Wavefront Sensor (CWS), developed by KIS, which is responsible for image stabilization and autofocus, the PCS was required to achieve a pointing accuracy better than 0.005" root mean square (rms) over extended periods to facilitate long-duration observations.

The Sunrise III telescope is a Gregory-type reflector with a 1-meter aperture, featuring a 234 mm central obscuration and an effective focal length of 24.2 meters. This configuration provides a field of view (FoV) of 3.4', corresponding to approximately 150 Mm on the solar

surface. The telescope directs light to the post-focus instrumentation platform (PFI), located above the telescope. The PFI houses the three scientific instruments and the CWS, and is responsible for distributing light among these four instruments. This distribution, performed by the Image Stabilization and Light Distribution Unit (ISLiD), must efficiently separate the different wavelengths in a photon-efficient manner to provide the highest number of available photons to each instrument.

While all the subsystems discussed thus far directly influence the optical performance, it is equally important to recognize the crucial role played by other subsystems, such as the electronics and software control. In particular, the Instrument Control System (ICS) is responsible for the management of the observatory, gathering housekeeping and issuing commands to the electronic units of each instrument. As will be elaborated in the following chapter, Sunrise III observations were designed to operate in a semi-autonomous manner through the use of pre-programmed timelines. This approach requires that all electronic systems function in synchrony, with minimal human intervention.

1.1.2 Science with Sunrise.

The absence of Earth's atmosphere opens the window for IR and UV observations and offers a level of image stability that cannot be achieved in ground-based observatories due to atmospheric seeing. However, these advantages are also present in spaceborne missions, such as the Spectro-Polarimeter and Narrowband Filter Imager aboard the Solar Optical Telescope of the Hinode mission (Kosugi et al. 2007, Tsuneta et al. 2008), or the Polarimetric and Helioseismic Imager aboard Solar Orbiter (SO-PHI) (Solanki et al. 2020, Müller et al. 2020), among many others. Nonetheless, spaceborne missions have strong restrictions regarding payload, mass and data rate.

The absence of these restrictions in balloon-borne observatories allows for a more complex and versatile instrumentation than the one present in space missions. The combination of these two factors, namely the absence of atmosphere and the complex and advanced instrumentation they can carry, places observatories such as Sunrise in an unique position, and provides them with unique perspectives on solar phenomena.

Many aspects of the physical processes driving our Sun remain unresolved. The mechanisms underlying various solar phenomena are still the subject of debate, ranging from the origin and removal of magnetic flux in the solar photosphere to the processes responsible for heating the chromosphere and corona, as well as the small-scale dynamics of solar plasma. The three instruments aboard Sunrise work in consonance to provide novel insights into these phenomena, and aim at helping the community solve some of the open questions of solar physics.

The magnetic field, present across multiple scales and heights, is the principal driver of solar activity. Understanding the magnetic field is essential for comprehending the processes that govern solar phenomena, energy distribution, and plasma dynamics. Numerous works direct their efforts to the study of the structures and evolution of magnetic fields. For instance, several works study the emergence of magnetic flux in the photosphere, such as, Danilovic et al. (2010) and Guglielmino et al. (2012), where they utilized Sunrise I IMaX

data to examine small-scale flux emergence events occurring within solar granules. Likewise, the processes responsible for magnetic flux removal are not fully known. Several studies, such as Zwaan (1987) and Guglielmino et al. (2012), have proposed mechanisms for flux removal in the photosphere; however, no model is favoured over the other by current observations.

A thorough 3-dimensional analysis of the magnetic fields is essential to study these events. The combination of spectropolarimeters and vector magnetographs aboard Sunrise, which are capable of measuring strong magnetic fields through the Zeeman effect, and detecting weaker, more turbulent (Bellot Rubio & Orozco Suárez, 2019) magnetic fields using the Hanle effect - particularly sensible in the UV - can provide a new and complete perspective of these events.

One of the scientific targets of Sunrise is the study of the upper atmosphere, whose dynamics and heating mechanisms are not yet completely understood. In fact, the transfer of energy from the lower layers to the chromosphere and corona is one of the open problems in stellar astrophysics. Several studies propose mechanisms in which the magnetic field plays a central role in this energy transfer. Some works suggest upward currents generated by the slow motion of plasma in the photosphere as a driving mechanism (Parker (1983), Pontin & Hornig (2020)), while others highlight heating processes induced by jets (Shibata et al., 2007) or magnetic vortex phenomena, such as twisted magnetic fields known as solar tornadoes (Wedemeyer-Böhm et al., 2012).

Although some observational signatures of these processes have been detected, the detailed characterization of these events requires higher spatial and temporal resolutions than those currently available. The high-cadence UV observations, where several spectral lines sensitive to the weaker magnetic fields of the chromosphere are present, combined with magnetic field maps of the photosphere and lower chromosphere provided by TuMag, and complementary observations of the Ca II infrared lines, provide Sunrise with the necessary tools to investigate these phenomena with unprecedented detail.

Sunrise also aims to provide novel insights into small-scale plasma dynamics. The Sun is highly dynamic, with structures evolving on timescales of minutes. Several studies propose that the magnetism in the quiet Sun is driven by the turbulent small-scale dynamics of the plasma (Petrovay & Szakaly (1993), Hotta et al. (2015), Rempel et al. (2023), among others). However, investigating these processes requires high spatial and temporal resolutions, which are often unattainable in ground-based observations. Similarly, other approaches to plasma dynamics, such as helioseismology (Gizon et al., 2010), also demand such high-resolution data. To address these challenges, Sunrise III conducted extended, highly stable due to the absence of atmospheric seeing, and uninterrupted observations lasting up to 6 hours, with the highest temporal resolution permitted by the (S/N) requirements.

In addition to these objectives, Sunrise will explore new and exciting areas, including the measurement of the polarized solar spectrum in the UV. This spectral region remains largely unexplored due to the technical challenges associated with its observation. Atmospheric absorption makes it impossible to observe this band from ground-based observatories, and it has yet to be measured by any space mission. SUSI is the first UV spectropolarimeter to acquire high-resolution data in this wavelength range.

Requirements	Value
Field of view	63'' x 63''
RMS wavefront error	$W \sim \lambda/14$
Spatial sampling	3 × 3 pixels
Plate scale	0.0378'' / pixel
Polarimetric efficiencies	$\epsilon_{1,2,3} \lesssim \frac{1}{\sqrt{3}}$
SNR ratio	$(\frac{S}{N})_0 \gtrapprox 1700$
Spectral resolution	< 9 pm
Spectral lines	Fe I 5250.2 Å, Fe I 5250.6 Å and Mg I b_2 5172.7 Å.
Time for a two-line observation	< 90 s

Table 1.1 Tumag scientific requirements.

1.2 The Tunable magnetograph: TuMag

TuMag is an FPI-based tunable imaging spectropolarimeter, capable of measuring the full Stokes vector across various spectral lines. This tunability allows TuMag to probe the magnetic field in both the photosphere and lower chromosphere, with high resolving power, thanks to its near-diffraction-limited imaging capabilities. The design of TuMag is inherited from IMaX, the imaging spectropolarimeter that flew aboard previous Sunrise missions. However, TuMag incorporates several advancements over its predecessor, including the addition of filter wheels for tunability between spectral modes and calibration systems, along with newly designed cameras and modulation packages.

In this section, we present an overview of the design of TuMag and its performance. It is important to note that this discussion will primarily focus on the instrument's optical design and performance—specifically its polarimetric, spectral, and imaging properties. The thermal design and control software, while crucial to the instrument's functionality, will not be covered here to avoid excessive length. Nonetheless, it is essential to acknowledge that these aspects are integral to TuMag's overall performance and represent a substantial portion of the effort contributing to its success.

1.3 TuMag's design and light path.

As a polarimeter, TuMag must be able to measure the full Stokes vector of the incoming light. To achieve this, it must generate four distinct modulation states and measure them in an almost simultaneously manner. As a spectrometer, TuMag must possess the capability to select specific wavelengths along multiple spectral lines. This selection process involves, first filtering the light with a pre-filter, which selects a "broad" spectral range, followed by an etalon that further narrows the bandpass within the selected range. Throughout this procedure, stringent requirements regarding polarimetric sensitivity (efficiency), spectral resolution, and imaging quality must be maintained. A summary of these requirements is

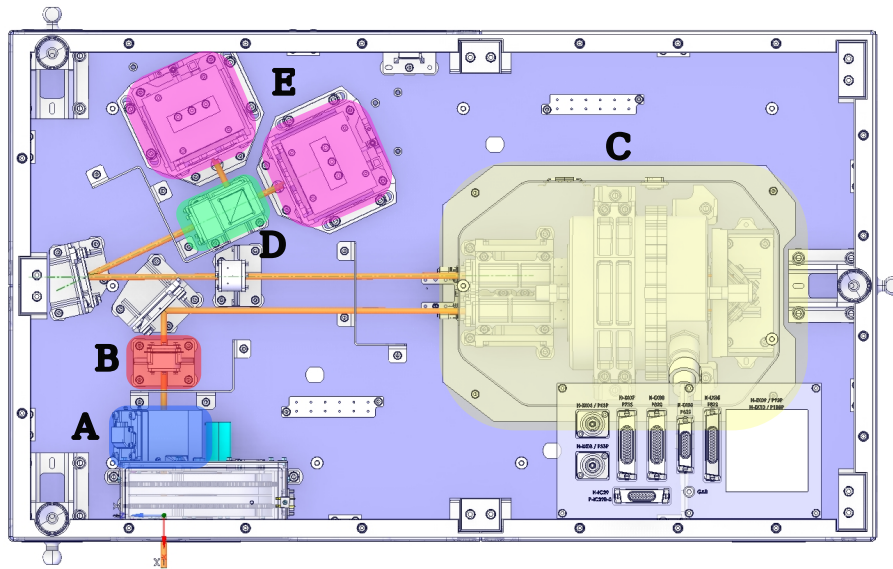


Figure 1.2 Schematic representation of the Tumag instrument. Some relevant optical devices in the light path (yellow line) are highlighted with a colored box and labeled with letters from A to E: A) Filter wheel, B) PMP, C) Etalon oven, D) beam-splitter and E) cameras. Image taken from TUMAG PAPER REF, reproduced with permission.

presented in Table 1.1.

Light is delivered to TuMag by the ISLiD system and subsequently re-imaged onto two cameras where the images are recorded. Before reaching the cameras, the light passes through all the different subsystems of the optical unit. The first components encountered by the light are a blocking prefilter and the filter wheels (box A in Fig. 1.2). The blocking prefilter, with a wide bandpass centered at 520 nm, is employed to eliminate unwanted spectral ranges. The filter wheels are comprised by a double-disk system (Sánchez et al., 2022) that houses the prefilters for selecting specific spectral lines and a series of calibration modules. Specifically, three prefilters are mounted on the second disk of the filter wheel, corresponding to the spectral lines Fe I 5250.2 Å, Fe I 5250.6 Å, and Mg I b_2 5172.7 Å. Additionally, the filter wheels include a PD plate, which is used to introduce a known defocus into the final image to facilitate image reconstruction techniques, along with a linear polarizer, a plate of micropolarizers, and a pinhole set, employed during calibration observations.

After passing through the filter wheels, the light is directed into the Polarization Modulation Package (PMP), a subsystem derived from the SO/PHI instrument (Álvarez-Herrero et al. 2018a, Solanki et al. 2020), highlighted with the red box in Fig.1.2. The PMP's primary function is to modulate the light to produce the different polarization states required to deduce the Stokes components. This is achieved using two liquid crystal variable retarders (LCVRs), which are oriented with their fast axes at 45° relative to each other. These LCVRs induce a retardance on the transmitted light that varies with the voltage applied across the crystals. The system can operate in two distinct modulation schemes: a vector modulation scheme, which generates four independent linear combinations of equally-weighted Stokes

components across consecutive observations, allowing for the retrieval of the full Stokes vector after demodulation; and a longitudinal modulation scheme, which generates only two modulations, providing information solely on the intensity and circular polarization.

Following modulation, the light is directed into a LiNbO₃ Fabry-Pérot etalon, highlighted in yellow in Fig.1.2 (box C). Likewise IMaX, the etalon operates in a collimated setup and with a double pass configuration (Álvarez-Herrero et al., 2006). In this configuration, after the light passes through the etalon once, it is redirected by a pair of mirrors to pass through the etalon a second time. This double-pass configuration significantly enhances spectral resolution by narrowing the transmission profile. The LiNbO₃ etalon tunes the resonance wavelength by varying the refractive index of the cavity through the application of high voltages (ranging from -4000 V to 4000 V). Compared to air-gapped etalons, these kind of etalons offer the advantage of having no moving parts, which is particularly beneficial for spaceborne or balloon-borne instruments. However, this advantage comes with the need for precautions to prevent discharges caused by air ionization.

The final optical element the light encounters before reaching the cameras is a polarizing beam splitter (green box C in Fig.1.2). At this stage, the light beam is divided into two orthogonal, linearly polarized components, each directed towards a different camera. This dual-beam configuration (Lites, 1987) is designed to minimize spurious signals induced by jitter of the gondola (see del Toro Iniesta (2003) for an extended discussion), as it effectively cancels fluctuations from Stokes I to the other Stokes parameters that may arise due to image motion or solar evolution (*i.e.* cross-talk).

Light then reaches the cameras, shown with pink boxes (boxes E) in the scheme, where images from both are recorded and stored. After mission recovery, the data is processed on-ground to combine images from the different cameras, modulation states, and spectral lines, ultimately deriving the scientific products. This processing and reduction of the data is accomplished using software specifically developed for TuMag, which will be extensively discussed in Chapter 2.

1.4 Instrument performance and verification.

All subsystems within the TuMag light path function collaboratively to deliver high-resolution spectroscopic data of the solar spectrum. To ensure data quality, TuMag underwent multiple verification and calibration processes, during which its spectral, polarimetric, and imaging properties were meticulously tested. These procedures, commonly referred to as end-to-end (E2E) calibration tests (see Álvarez Herrero et al. (2022) for a detailed description of the tests), were conducted at various stages of the mission. Specifically, they were performed during the assembly, integration, and verification (AIV) activities with the stand-alone instrument at INTA facilities in Madrid, Spain; during the AIV phase of the PFI platform at MPS facilities in Göttingen, Germany; and during the TuMag AIV phase in the Sunrise III mission at ESRANGE facilities in Kiruna, Sweden. These tests were designed not only to validate the instrument's capabilities but also to measure critical parameters such as the tuning constant of the etalon, modulation matrices, and best-focus position—each

of which is vital for the optimal operation of TuMag and the subsequent data processing. We will now delve into the details of the imaging, spectral and polarimetric properties of the instrument as well as the verification processes and results, as the two are intimately related.

1.4.1 Imaging performance.

TuMag captures photons using two custom-made cameras (Orozco Suárez et al., 2023) equipped with GPIXEL back-illuminated GSENSE400BSI detectors, each featuring a $2k \times 2k$ pixel array, and specifically designed to meet TuMag's scientific requirements. These cameras provide a broad FoV of $63'' \times 63''$, sufficient to encompass an entire medium-sized active region, with a plate scale of $0.0378''/\text{pixel}$.

In order to fulfill the requirement of the wavefront error of $W \sim \lambda/14$, the instrument must have means to correct for the additional aberrations introduced by the telescope, the image stabilization and light distribution (ISLiD) system and uncorrected jittering. For this purpose, TuMag is equipped with a PD plate in the filter wheel that allows for the assessment of the PSF during the observations to apply image restoration techniques during the data processing.

The imaging E2E tests involved projecting several targets at the F4 focus, including a USAF test target, star targets, and a grid, observed both with and without the PD plate. These targets were utilized to evaluate the MTF and to assess the resolving power of TuMag. The PD measurements enabled verification of the wavefront error (WFE) derived from the MTF and an evaluation of the image quality following image restoration.

The USAF target^{*} consists on a series of horizontal and vertical line pairs (lp) arranged in sets of three with varying resolutions. Identifying the highest resolution group observable with TuMag allows for a fast diagnostic of the instrument resolution and performance. In fig. 1.3, measurements of group 4 and 5 (and higher) of the USAF target are shown for both cameras and the three pre-filters. The second set of group 5 (highlighted in a white box), which corresponds to 35.9 lp/mm in the target and 24.3 lp/mm in the image, is of special interest since its close to the Airy disk radius (26.4 lp/mm) and therefore close to TuMag's resolution limit.

The results show a better optical performance for the 517 nm pre-filter than the other two pre-filters. The USAF 5.2 set is clearly resolved fo this pre-filter in both cameras showing almost no difference between vertical and horizontal resolutions. However, results for the 525 nm prefilters exhibit a worsening of the resolution, with the same set being hardly resolved in the horizontal direction in both prefilters.

However, a more precise evaluation of the optical performance can be achieved from the MTFs. Figure 1.4 shows the MTFs computed with a slit target (see Huang et al. (2013) for a description of the MTF computation method) during the E2E tests performed in December 2021 at INTA facilities. These results agree with the diagnostic carried with the USAF tests: the 517 nm pre-filter shows a good performance in both directions, with values above the

^{*}The 1951 USAF target from Thorlabs Inc, model: R1DS1N.

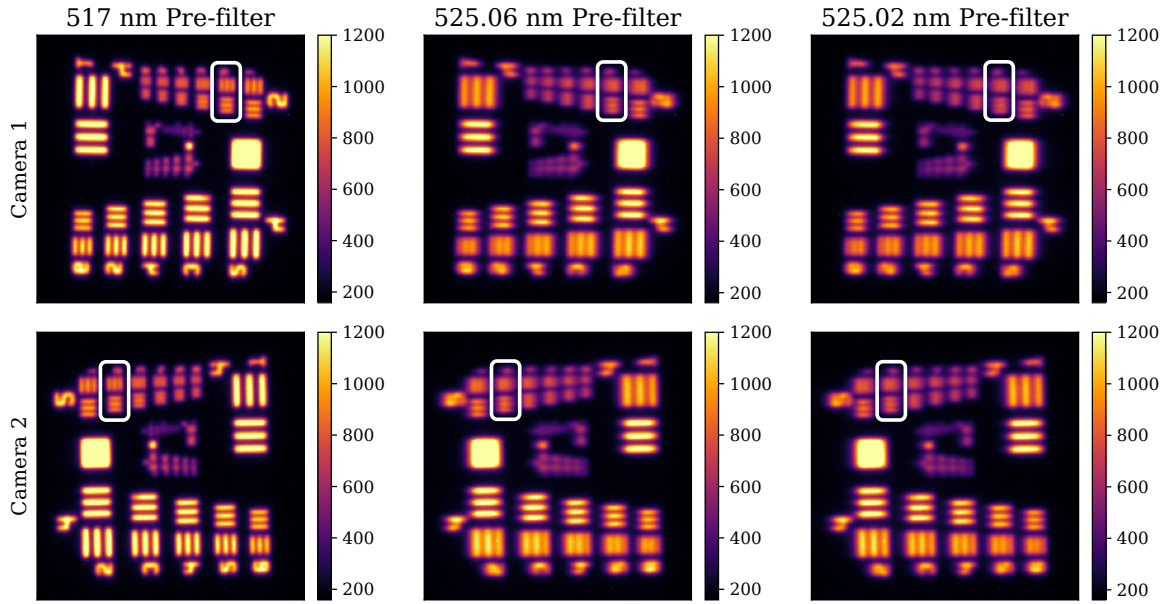


Figure 1.3 USAF target measurements for both cameras and the three pre-filters performed during E2E tests at INTA facilities on December 2021. The white boxes highlight the second element of the test group 5 (35.9 lp/mm). The scale of the images is set in digital counts.

expected behaviour. Meanwhile, 525 pre-filters exhibit a large difference between different directions with an important drop in vertical resolution in both cases. This observed astigmatism is attributed to the etalon and physical deformations of the pre-filters caused by the mechanical method used to secure and tilt them. This effect is particularly noticeable in the iron pre-filters due to the higher angles of incidence required for their tuning.

The comparison of the obtained MTF and the diffraction-limited one allows for an estimation of the Strehl ratio, and consequently the wavefront error (see section ??).

Table 1.2 shows the results for the Strehl ratios and WFE derived from this computation. All values, except for the horizontal resolution in camera 1 of the 517 nm prefilter are lower than the $\lambda/14$ set as a requirement. However, images can always be restored if $WFE \gtrapprox \lambda/5$ (Vargas Dominguez, 2009) if the PSF is known, thus the need for the inclusion of PD capabilities in the instrument. Furthermore, PD techniques not only allow us to enhance the optical performance of the instrument but also evaluate the optical performance during the calibrations in order to verify the results obtained through the computation of the MTF.

Figure 1.5 shows the measurements and results of the PD analysis for the 517 nm pre-filter and the camera 1. The measurements were carried out during the final E2E tests performed at Kiruna on April 2024 using the random dot target (left and central columns of the figure). The measurements consist on 5 sets of focused-defocused pairs of images. The PD algorithm is run over a zoomed-in region of 600 pixels in sub-patches of 128x128 pixels. The mean Zernike coefficients are shown in the top right panel, where the error has been computed as the standard deviation between different sub-patches. A 2D representation of the rms WFE is also shown in the bottom right panel.

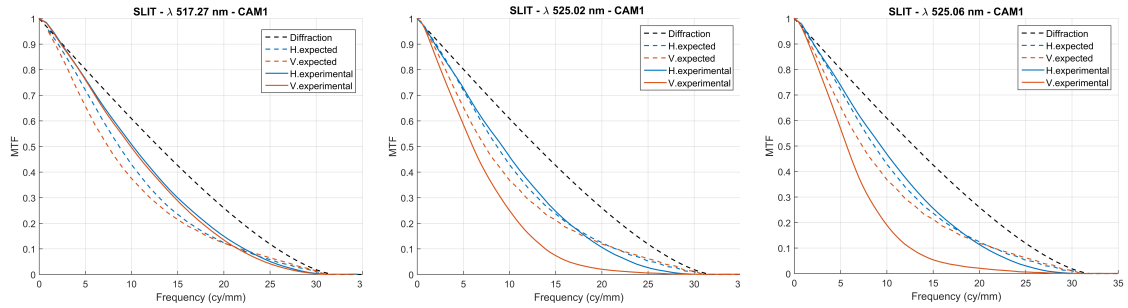


Figure 1.4 MTFs derived for camera 1 (very similar results for camera 2) for the three pre-filters from measurements of the stand-alone AIV phase performed at INTA in December 2021.

Pre-filter and camera	Strehl ratio Vertical	Strehl ratio Horizontal	WFE Vertical	WFE Horizontal
517 nm - Cam 1	0.782	0.826	$\lambda/12.7$	$\lambda/14.5$
517 nm - Cam 2	0.761	0.806	$\lambda/12.1$	$\lambda/13.5$
525.02 nm - Cam 1	0.436	0.725	$\lambda/6.9$	$\lambda/11.1$
525.02 nm - Cam 2	0.405	0.726	$\lambda/6.6$	$\lambda/11.1$
525.06 nm - Cam 1	0.451	0.764	$\lambda/7$	$\lambda/12.1$
525.06 nm - Cam 2	0.444	0.736	$\lambda/7$	$\lambda/11.3$

Table 1.2 Optical performance evaluated from the MTFs obtained with the slit target at December 2021 E2E tests.

The PD analysis indicates a small amplitude for most aberrations, with coefficients beyond Z15 approaching zero, except for the spherical aberration (Z_{11}, Z_4^0) which is the dominant contribution to the rms wfe. However, the results exhibit significant dispersion, as reflected by error bars that reach values up to 0.025λ for the first coefficients. Both the defocus and astigmatism are pretty low (Zernike indexes 4, 5 and 6, Z_2^0, Z_2^{-2} and Z_2^2 , respectively), agreeing with the results obtained from the MTF analysis which showed a good resolution in both vertical and horizontal directions. The overall rms WFE obtained from this analysis is $\lambda/11.4$. It is important to note that the PD analysis shown here was carried out at the final stages of the calibration campaign, with TuMag mounted on the PFI and the light being fed to the instrument through the telescope and ISLiD system, whereas the MTF determination was conducted in the stand-alone AIV phase, without the aberrations introduced by these systems. Nevertheless, both analyses agree on a WFE better than $\lambda/10$, indicating very high optical quality, despite the fact that the FPI of TuMag operates in a collimated configuration, which is known to degrade optical performance (Scharmer, 2006).

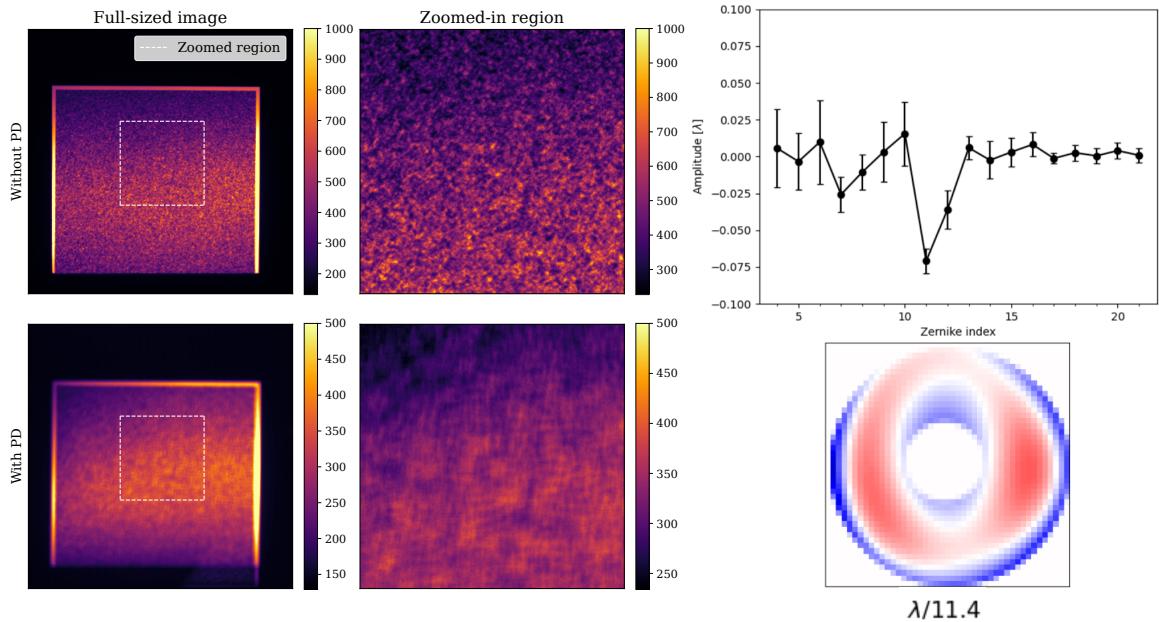


Figure 1.5 Random dot target measurements of the 517 nm pre-filter with the camera 1 and without the PD plate (left and central columns) taken during the Sunrise III AIV phase in Kiruna on April 2024. The right column shows the Zernike coefficients obtained from the PD analysis in the top panel and the 2D representation of the rms WFE. The PD analysis has been carried out by F. J. Bailén, reproduced with permission.

1.4.2 Spectral performance.

TuMag filters wavelengths through a sequential process, beginning with a broad blocking pre-filter that eliminates unwanted regions of the solar spectrum, and followed by a second narrow-band pre-filter that is tuned to the three selected spectral lines. Finally, the LiNbO₃ Fabry-Pérot etalon is encharged of selecting a very narrow band around specific wavelengths along the spectral lines. The narrow-band pre-filter and the etalon are critical to TuMag's spectroscopic performance and require careful evaluation during calibration.

The three TuMag pre-filters were custom-manufactured by MaterionTM and have a full width at half maximum (FWHM) close to 1 nm. They are centered near the rest wavelength of the three spectral lines at normal incidence, with a peak transmission exceeding 80% in all cases. Each pre-filter was tuned by adjusting the incidence angle to align the peak transmission wavelength with the spectral line core. This process was performed using a coelostat at the INTA facilities, where the rest positions in volts of the spectral lines were determined. The Fe I 5250.2 Å line was found at 2129 V, the Fe I 5250.6 Å line at -2507 V, and the Mg I *b*₂ 5172.7 Å line at -2245 V. While this tuning was successful, particularly for the iron lines, the spectral position of the pre-filters was found to be highly sensitive to illumination conditions. This sensitivity was evident from the shifts observed in the pre-filter measurements during the various stages of the assembly process. As illustrated in the left column of Fig. 1.6, the variation in the spectral position of the pre-filters is not sufficient

Property	Value
Reflectivity	0.892
Thickness	281 μm
FWHM (double-pass)	0.8
Tuning Constant	3300 V/ \AA

Table 1.3 Tumag Fabry-Pérot specifications.

to cause the spectral line to be blocked by the pre-filter, but it may result in the spectral line falling on the wing of the pre-filter during observations.

TuMag's etalon (see Table 1.3) operates in a collimated setup with a transmission profile with a FWHM of 0.87 pm (in the double-pass configuration), thus achieving a spectral resolution that exceeds the required 9 pm. Observations of an iodine cell illuminated with a diode were conducted to verify the transmission profile's shape and accurately assess the tuning constant. The right column of Fig. 1.6 presents, in orange, the iodine cell measurements obtained during the assembly, integration, and verification (AIV) phase of TuMag's integration into the Post Focal Instruments (PFI) platform, which took place at the Max Planck Institute for Solar System Research (MPS) in Göttingen, Germany, in November 2023. Additionally, the dark blue line in the figure represents a simulation of the iodine spectrum observations. This simulation was generated using an analytical model of the transmission profile of collimated etalons (see section ?? for a detailed overview of the model). The results confirm that the spectral resolution achieved in the iodine cell observations is consistent with the estimated 0.87 pm resolution. Furthermore, these observations enabled the calculation of the etalon's tuning constant by identifying the corresponding line cores between the simulation and observation and applying a least squares fitting to establish the relationship, which was measured in 3300 V/ \AA .

An observation of the solar spectrum with the 517 nm pre-filter, conducted at INTA facilities in December 2021 during the end-to-end calibration tests, is presented in Fig. 1.7, along with the corresponding pre-filter measurement. The magnesium line core is detected at approximately -2200 V using the primary order of the etalon and reappears around 3750 V with a secondary order. A fitting of the solar spectrum[†] is also shown for both orders. These results reveal significant contamination from the secondary order near the pre-filter's minimum transmittance. At around 0 volts, the observed spectrum (orange line) is a composite of contributions from both the primary (red line) and secondary (green line) orders. This contamination is particularly relevant for data processing, as continuum measurements of the magnesium line are typically conducted at -80 V. The broader profile of the magnesium line necessitates continuum measurements farther from the line core, making it more susceptible to this contamination. In contrast, the narrower iron lines do not require such extensive offsets for continuum measurements and are thus less affected.

[†]Reference

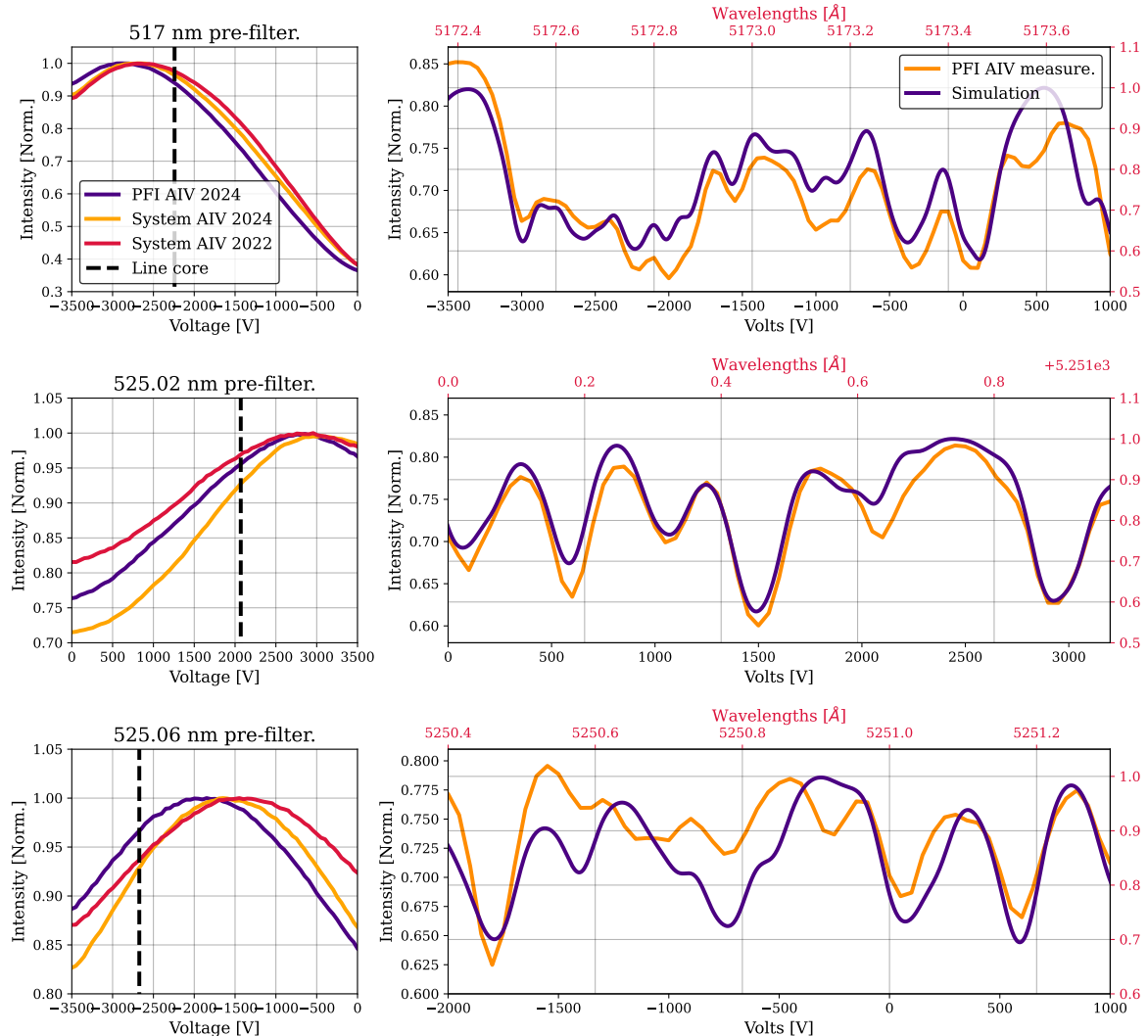


Figure 1.6 TuMag spectroscopic calibration results. Each row shows results for the 517 nm, 525.02 nm and 525.06 nm pre-filters, from top to row. The left column shows measurements of the pre-filters carried out with a flat LED on different stages of the AIV phases. The right column shows the fit of the I_2 cell observation with a simulation employing an etalon with a reflectivity of 0.892 (FWHM ~ 0.87). Note that the absolute value of the wavelengths of the simulation (red axis) might be shifted with respect to real values due to unknown conditions of the reference.

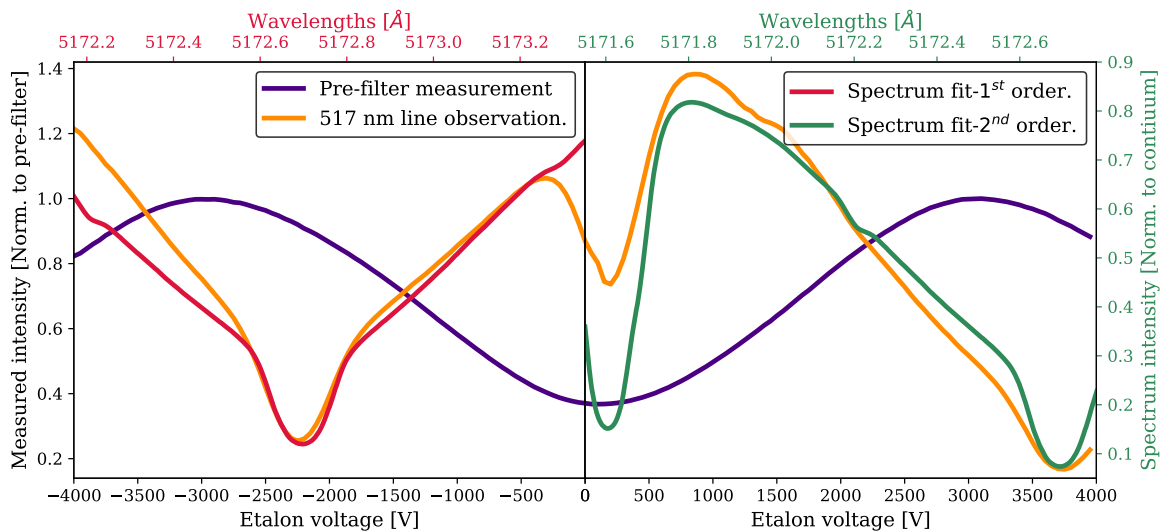


Figure 1.7 Results of the spectroscopic calibration during the end-to-end calibrations of the AIV phase of 2021. The dark blue curve represents the measurement of the 517 nm pre-filter, alongside an observation of the magnesium line using the coelostat at INTA facilities, shown in orange. Two different fits of the solar spectrum are overplotted on the figure. The red line represents a fit to the primary etalon order (negative voltages), while the green line corresponds to a fit to the second etalon order (positive voltages).

1.4.3 Polarimetric performance.

TuMag modulates the incoming light through a PMP composed of two anti-parallel LCVRs. These devices can modify the phase retardance induced to the light that goes through them by changing the alignment of their molecules when subject to a voltage potential. Their advantages for airborne instruments lie in their lightweight and compact design, the low voltage required for operation ($[0 - 10]$ V), and their efficiency in producing either four linearly independent modulation states for full-Stokes polarimetry or only two states for measuring the longitudinal component of the magnetic field through Stokes V. This versatility is a specific advantage of LCVRs, not found in quarter-waveplate-based PMPs (Pillet et al., 2004).

TuMag's polarimetric measurement approach is divided into the two modulation schemes already mentioned: vectorial and longitudinal. In the vectorial scheme, four linearly independent modulation states are generated in rapid succession by the PMP, enabling the calculation of the full Stokes vector. Conversely, the longitudinal approach generates only two modulation states, providing information on just two components. This modulation is designed to compute Stokes V by determining the quantities $I \pm V$.

Both modulation schemes are required to operate under an optimal modulation scheme. Such a scheme is defined by a modulation matrix with the following polarimetric efficiencies: $\varepsilon_{opt} \geq [1, \frac{1}{\sqrt{3}}, \frac{1}{\sqrt{3}}, \frac{1}{\sqrt{3}}]$. The selected modulation scheme was based on the retardances outlined in Table 1.4. A thorough calibration of the liquid crystal variable retarders (LCVRs)

Spectral lines	Modulation	Vectorial				Longitudinal	
		I1	I2	I3	I4	I1	I2
525 & 517 nm	LCVR1 retardance	225°	225	315°	315°	180°	180°
525 & 517 nm	LCVR2 retardance	234.74°	125.26°	54.74°	305.26°	90°	270°
525 nm	LCVR1 voltage	2.291	2.533	1.992	1.947	2.761	2.761
	LCVR2 voltage	2.375	3.360	6.433	2.016	4.723	2.186
517 nm	LCVR1 voltage	2.343	2.580	2.031	1.972	2.797	2.797
	LCVR2 voltage	2.371	3.416	6.548	2.051	4.77	2.206

Table 1.4 Tumag LCVR retardances and corresponding voltages for both modulation schemes and the three pre-filters. Note that a single value is provided for both iron pre-filters.

was conducted to accurately determine the voltages necessary to produce the specified retardances (Álvarez-Herrero et al., 2018b).

Considerations on the (S/N) are critical for ensuring the required polarimetric sensitivity. Achieving an S/N of 10^3 in the Stokes measurements imposes a requirement of $S/N \approx 1200$ for each modulation measurement per camera. This calculation assumes near-optimal polarimetric performance, and takes into account the dual-beam polarimetry technique, which increases the S/N by a factor of $\sqrt{2}$ when combining data from the two cameras. A single shot of the cameras is insufficient to reach these S/N values, as the sensors do not have enough capacity in their electron wells. To address this, multiple exposures are captured and subsequently summed during each observation. This *accumulation* strategy, extensively tested and employed in various polarimeters (e.g., Elmore et al. 1992, Martínez Pillet et al. 1999, Lites et al. 2001), has proven compatible with image reconstruction techniques (González & Kneer, 2008; Van Noort & van der Voort, 2008). It allows for adjusting S/N levels depending on the scientific objectives of the observation, balancing between velocity and polarimetric sensitivity.

However, in order to fulfill the polarimetric sensitivity requirements, the modulation matrix of the instrument must be carefully addressed during the polarimetric calibrations. Any deviation in the computation of the modulation matrix, will introduce spurious signals in the polarization measurements, known as cross-talk. The polarimetric calibration involves a series of measurements using a light beam with a known polarization state, generated by a rotating linear polarizer and a rotating quarter-waveplate. By varying the positions of these two devices, 40 different input polarization states were produced and measured with three pre-filters. These measurements allowed for the precise determination of the modulation matrix by solving the system of equations (??), where the only unknown is the modulation matrix \mathbf{M} , as both the measured modulation and the Stokes components of the incoming light are known.

The results of the polarimetric calibration performed during the end-to-end (E2E) tests at INTA in December 2021 are presented in Fig. 1.8. The figure shows the results for camera one; however, camera two demonstrated nearly identical efficiencies. The polarimetric efficiencies across the entire field of view (FoV) exceed the required thresholds

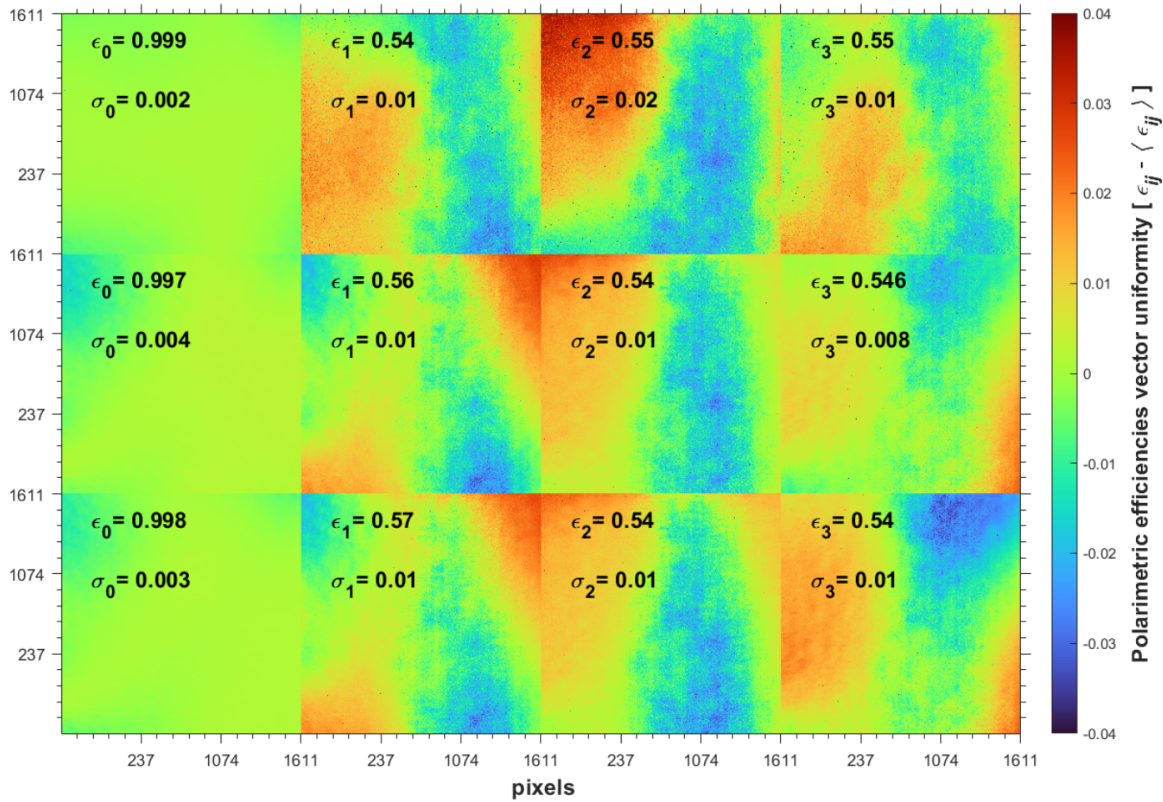


Figure 1.8 Polarimetric efficiencies for camera 1 and the three pre-filters (from top to bottom, the different rows show the results for 517 nm, 525.02 nm, and 525.06 nm). The different columns correspond to the efficiencies of the different Stokes components. The colormap measures the differences in efficiencies along the FoV. Results obtained during the E2E tests performed at INTA in December 2021, during the stand-alone AIV phase.

$\varepsilon_{req} \geq [0.95, 0.45, 0.45, 0.45]$, and approach the optimal values. Furthermore, efficiency variations along the FoV are generally low, with standard deviations lower than 0.01. This homogeneity of the polarimetric performance makes the data reduction easier as no special treatment is required for specific regions.

CHAPTER 2

TUMAG'S PIPELINE AND DATA.

INtro? tumag flew on bla vla. The data was recovered bla bla, The reduction process started on bla bla and is ongoing right now bla bla.

2.1 TuMag's observing modes

TuMag operates through a series of so-called observing modes. The observing modes are a list of pre-configured settings for the observations that fullfill different scientific puprposes and are meant to allow an almost automatic operation of the instrument during flight.

A summary of the properties for each observing mode is provided in Table 2.1. There are four distinct modes designed to observe the magnesium line. Mode 0s performs a fast, extended scan of the spectral line using 12 wavelength samples: [-40, -30, -20, -10, 0, 10, 20, 30, 40, 50, 60, 65]*, with one modulation and two accumulations to maximize scanning speed. Mode 0p is similar to mode 0s but employs a full-vector modulation scheme, requiring 16 accumulations to ensure the required SNR. Mode 1 provides a shortened scan of the magnesium line, with measurements taken at [-30, -20, -10, -5, 0, 5, 10, 20, 30, 65],

*Sampling positions are given relative to the line core.

Observing mode	Spectral lines	N_λ	N_P	N_a	N_c	$t_{eff}(s)$	(S/N)
0s	Mg I b_2 5172.7 Å	12	1	2	1	6.3	500
0p	Mg I b_2 5172.7 Å	12	4	16	1	37.62	1000
1	Mg I b_2 5172.7 Å	10	4	16	1	31.81	1000
2	Fe I 5250.2 Å, Fe I 5250.6 Å	8	4	16	1	23.4	1000
3	Fe I 5250.2 Å, Fe I 5250.6 Å	5	2	20	1	10.04	1000
4	Mg I b_2 5172.7 Å	3	4	10	10	54.01	2500
5	Fe I 5250.2 Å, Fe I 5250.6 Å	3	4	10	10	53.60	2500

Table 2.1 Scientific observing modes. From left to righ, the columns are: observing mode identiicator, measured spectral lines, number of wavelengths, of modulations, of accumulations, of cycles, the total timeand the polarimetric SNR.

also utilizing a vectorial modulation scheme. Finally, mode 4 is a "deep" magnetic mode, featuring a highly reduced scan with only three samples at [-10, 0, 10], but with increased accumulations and cycles to enhance polarimetric sensitivity.

Three observing modes are configured for the iron lines. Mode 2 employs a vectorial modulation scheme applicable to both iron lines, with sampling at [-12, -8, -4, 0, 4, 8, 12, 22] pm. Mode 3 uses a longitudinal modulation scheme, measuring only Stokes I and V, with samples taken at [-8, -4, 4, 8, 22] pm. Lastly, mode 5 closely resembles mode 4, but is configured for the iron lines, with sampling at [-8, 0, 8] pm. The only difference between these two modes is the sampling scheme.

Although most of the parameters are set up by the observing mode and cannot be changed, there are some configurable parameters that allow to slightly modify the observing modes to fit the specific goal of a particular. These parameters are the following:

Solo estos? o había más?

- ✿ λ_{rep} : A parameter that allows to repeat all the observations carried out at every spectral position before changing wavelength. This parameter is employed for flat-field observations (see the following section). By default is set to 1.
- ✿ Etalon offset : A parameter that allows for the introduction of a global shift to the spectral sampling by offsetting the absolute voltages (and thus, wavelengths) of the scan. This parameter was used to center the spectral line in shorter observing modes affected by solar rotation or other effects that might shift the spectral position. The default value is set to 0 V.
- ✿ N_a : Even though the number of accumulations is fixed in nominal observing modes, this parameter was set as configurable in order to allow modifications for faster observations when needed. The default value depends on the observing mode.

Figure 2.1 presents a schematic representation of the voltage ranges for the observing modes when converting spectral sampling to volts. The black lines indicate the voltage boundaries that cannot be surpassed during an observation due to technical constraints. These limits are set at ± 3750 V as the maximum and minimum values, with an additional limitation at 0 V, since a polarity change poses technical challenges that could not be addressed within an observation mode. These restrictions are significant in two cases: firstly, for Magnesium observation modes, specifically modes 1 and 0, where the continuum measurement is positioned as far from the core as possible, at -80 V, due to the 0 V crossing limitation. Secondly, these constraints are relevant when applying an etalon offset to shift the spectral positions of a particular observing mode, as the offset cannot cause the final positions to exceed these boundaries.

2.1.1 Calibration modes

An additional type of observing modes are also designed aimed at carrying out calibration observations. These calibration observing modes are more flexible than scientific ones, and

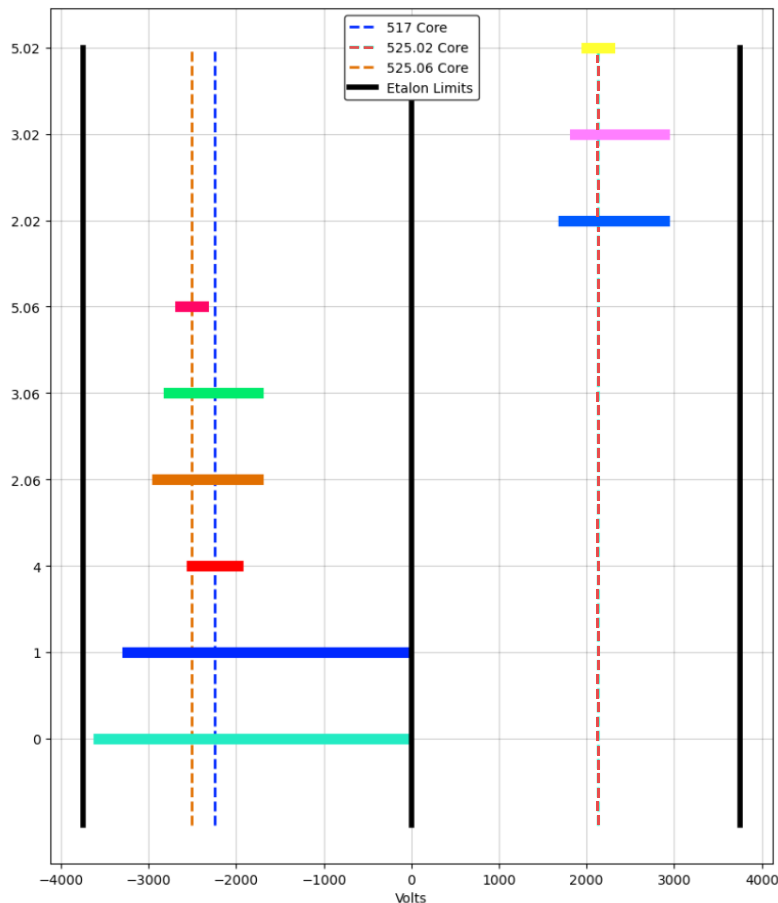


Figure 2.1 Schematic representation of the voltage range covered by all observing modes. The dashed lines indicate the position of the line core as measured during the E2E tests performed at INTA in December 2021. The black lines represent the voltage limits that cannot be crossed in an observing mode.

allow for the configuration of several parameters to match the observations to the aim of the scientific observation.

2.1.1.1 Flat-field observations

One of the essential calibration procedures in any telescope-based astronomical observation is the acquisition of flat-field images. These observations are designed to measure intensity variations across the FoV, which arise from several factors, including intensity gradients induced by the etalon, dust particles, or pixel efficiency variations, among other sources. The aim is to capture a region with no discernible structure, ideally producing a uniformly flat intensity distribution. However, achieving such flat-field observations is not always straightforward, particularly for certain instruments. While ground-based telescopes can utilize twilight periods to observe areas of the sky devoid of stars, space-borne or balloon-borne solar telescopes, such as Sunrise III, are unable to do the same and must look for alternative methods.

In Sunrise III, flat-field images are generated by deliberately blurring the solar image through rapid movements of the mirror. This process effectively removes any solar structure from the FoV when averaging out multiple blurred observations, resulting in a flat-field

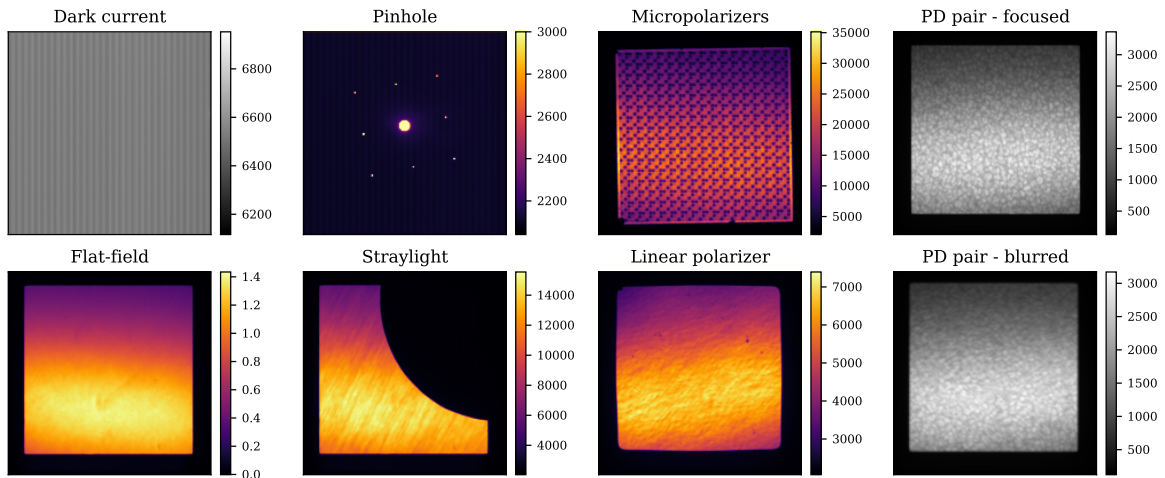


Figure 2.2 Examples of calibration observations. All images, with the exception of the flat-field, are presented in their raw format, without any manipulation or correction applied. The flat-field observation depicted corresponds to the first modulation of the continuum measurement obtained during a flat-field observation corresponding to observing mode 1. All data are belong to camera 1, and the colorbar is calibrated in digital counts save for the flat-field which is normalized to its mean value.

image devoid of solar features.

In the case of TuMag, flat-field observations are performed using a modified version of the nominal observing mode, where the λ_{rep} is set to 4. Additionally, multiple consecutive instances (N_{reps}) of these observations are executed, typically 5 or 7. During data processing, a single flat-field is generated for each wavelength position and modulation state by averaging all corresponding observations.

Figure 2.2 shows an example of a flat-field observation, for one camera, modulation and wavelength (bottom left panel). The image shows a clear deviation from flatness in the measurement, primarily due to the etalon intensity gradient, which accounts for the change in intensity between the brighter bottom half and the darker top half, and some minor inhomogeneities over the FoV.

2.1.1.2 Dark-current observations

A second critical calibration procedure for any observation involving electronic cameras is the measurement of dark current. In the absence of incident photons, electrons within the camera's wells can still be randomly excited. This spontaneous excitation can be incorrectly interpreted as photon-induced counts when analyzing the data. Dark current observations are designed to characterize these random electronic excitations, which are primarily influenced by the camera's physical conditions, particularly temperature, so that they can be accurately subtracted from the final images.

For TuMag, dark current calibration involved capturing a series of 50 images with $N_a = 50$ with no light entering the instrument. As with flat-field observations, a single dark

current frame for each camera is generated by averaging all individual observations. In the top left panel of fig. 2.2 a dark current shot is depicted, characterized by the vertical strips pattern.

2.1.1.3 Linear polarizer and micropolarizers observations.

TuMag's filter wheels are equipped with two targets designed to assess the instrument's polarimetric performance: a linear polarizer and a set of micropolarizers. Both targets are situated in the first filter wheel and are used in conjunction with the three distinct prefilters located in the second filter wheel. The linear polarizer serves to evaluate the polarimetric calibration, particularly by quantifying the level of cross-talk, as no circular polarization should be detected when using this target. The micropolarizers provide a more complete assessment, as they consist of multiple linear polarizers oriented at different angles.

Observations with this targets are carried with the three prefilters, at a single wavelength, located in the continuum of each line. For each measurement, a vectorial modulation scheme is employed that allows for the derivation of the four stokes parameters. In the third column of figure 2.2 observations of both targets are shown.

2.1.1.4 Pinhole Observations.

Another calibration target included in the filter wheels is the pinhole target. This target blocks most of the light reaching the instrument, except for a few small holes arranged in a square-like pattern across the FoV, as shown in the top panel of the second column of figure 2.2. A larger hole is located at the center of the FoV, surrounded by eight smaller holes that trace a square with the central hole at its midpoint. These observations serve various purposes, including image alignment, detecting the presence of ghost images, or identifying etalon reflections, among other uses.

Pinhole observations are conducted similarly to those with polarizers, that is, in combination with the three prefilters at a single wavelength (the continuum of each line), but without applying any modulation.

2.1.1.5 Straylight target.

Not all the light that reaches the detector is necessarily the intended signal for a given observation. Some unwanted light, primarily originating from internal reflections along the optical path, may also reach the instrument. This unwanted contribution, known as straylight, contaminates the measurements by reducing contrast, lowering the S/N, and generally degrading the spectral, optical, and polarimetric performance of the instrument.

To address this contamination, TuMag performed a series of observations using a target that blocks part of the FoV (see the bottom panel of the second column of figure 2.2). By analyzing the dark region in these observations, it becomes possible to measure and model the straylight reaching the instrument, allowing for its subsequent removal from the data.

2.1.1.6 Prefilter scans.

TuMag observations are very sensible to spectral shifts either from the pre-filters or from the observed spectral line position. The shift of the pre-filters can happen due to changes in the physical conditions of the filter wheels such as changes in temperatures which spectrally shift the behavior of the pre-filters. The position of the pre-filter greatly affect the measurements as it reduces the intensity of the measurements that are obtained in the wings of the pre-filter. Due to solar rotation, or changes in the conditions of the etalon, although these are less likely, the spectral position at which the spectral lines are recorded can change. This effect is specially important in observing modes that require great spectral accuracy, such as the deep modes, where only three spectral positions close to the line core are employed.

In order to verify the spectral behaviour of the prefilter, as well as the position of the spectral line, a series of observations were carried out, usually before and after the scientific observations, where a spectral scan with a rich spectral sampling was taken for all the pre-filters employed in the observation. These scans, measure the voltage range of the specific line with a sampling of **100V** and without modulating.

PLOT of the prefilters.

2.1.1.7 Phase diversity.

Lastly, TuMag is equipped with the capability to perform phase diversity for image reconstruction. As discussed in previous chapters, applying image reconstruction techniques is essential to meet the optical quality requirements. To this end, TuMag includes a PD plate in the first filter wheel that introduces a known defocus in the images. Capturing images with and without this plate enables the computation of the instrument's PSF, which can then be deconvolved from the data.

PD measurements require quasi-simultaneous pairs of aberrated and unaberrated images. Therefore, TuMag's PD observations consist of a series of 32 or 40 rapid, non-accumulated shots with the PD plate, followed by a corresponding series without the PD plate. The feasibility of this sequential scheme for phase diversity techniques has been confirmed in Bailén et al. (2022). A pair of focused-defocused images of quiet-sun observations is shown in the last column of figure 2.2.

2.2 Pipeline

2.2.1 Darks and flat fields

2.2.2 Blueshift

2.2.3 Demodulation and dual beam

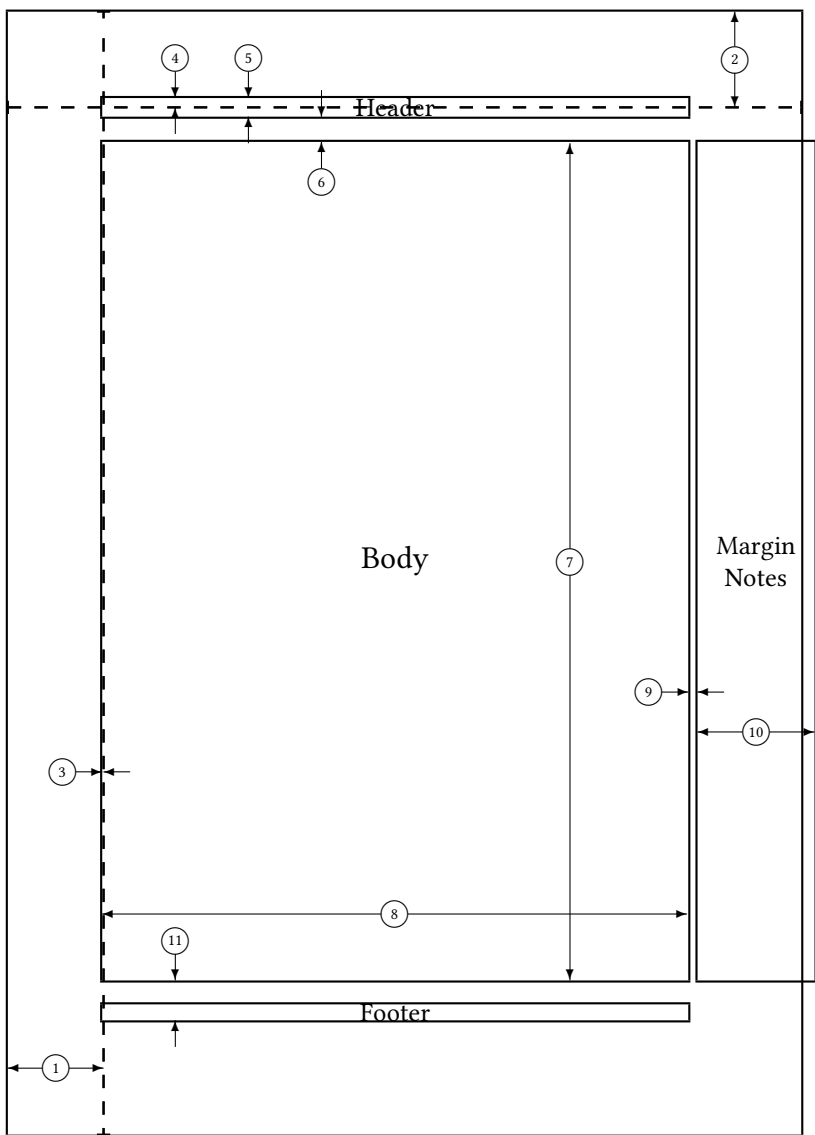
2.2.4 Cross Talk

BIBLIOGRAPHY

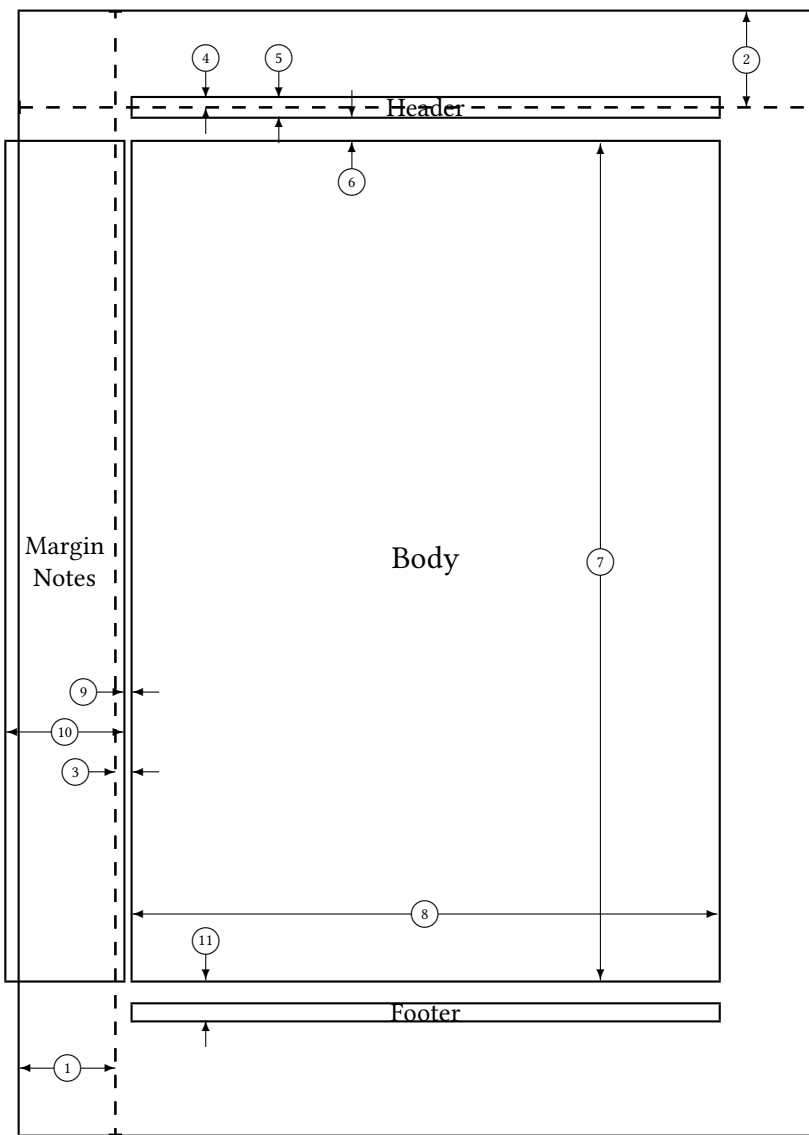
- Álvarez-Herrero, A., Belenguer, T., Pastor, C., et al. Lithium niobate fabry-perot etalons in double-pass configuration for spectral filtering in the visible imager magnetograph imax for the sunrise mission. *Space Telescopes and Instrumentation I: Optical, Infrared, and Millimeter*, SPIE, 797–812 (2006).
- Álvarez-Herrero, A., Parejo, P. G., & Silva-López, M. Fine tuning method for optimization of liquid crystal based polarimeters. *Optics Express* **26**, 12038 (2018).
- Álvarez-Herrero, A., Parejo, P. G., & Silva-López, M. Fine tuning method for optimization of liquid crystal based polarimeters. *Optics Express* **26**, 12038 (2018).
- Álvarez Herrero, A., Garranzo-García, D., Núñez, A., et al. End-to-end tests of the tumag instrument for the sunrise iii mission. *Ground-based and Airborne Instrumentation for Astronomy IX*, SPIE, 791–802 (2022).
- Bailén, F. J., Orozco Suárez, D., Blanco Rodríguez, J., & del Toro Iniesta, J. C. Performance of Sequential Phase Diversity with Dynamical Solar Scenes. *Astrophys. J. Suppl.* **263**, 7 (2022).
- Bellot Rubio, L., & Orozco Suárez, D. Quiet sun magnetic fields: an observational view. *Living Reviews in Solar Physics* **16**, 1 (2019).
- Danilovic, S., Beeck, B., Pietarila, A., et al. Transverse component of the magnetic field in the solar photosphere observed by sunrise. *The Astrophysical Journal Letters* **723**, L149 (2010).
- del Toro Iniesta, J. C. (2003), Introduction to spectropolarimetry (Cambridge university press).
- Elmore, D. F., Lites, B. W., Tomczyk, S., et al. Advanced stokes polarimeter: a new instrument for solar magnetic field research. *Polarization analysis and measurement*, SPIE, 22–33 (1992).
- Gizon, L., Birch, A. C., & Spruit, H. C. Local helioseismology: three-dimensional imaging of the solar interior. *Annual Review of Astronomy and Astrophysics* **48**, 289 (2010).
- González, N. B., & Kneer, F. Narrow-band full stokes polarimetry of small structures on the sun with speckle methods. *Astronomy & Astrophysics* **480**, 265 (2008).

- Guglielmino, S., Pillet, V. M., Bonet, J., et al. The frontier between small-scale dipoles and ephemeral regions in the solar photosphere: emergence and decay of an intermediate-scale bipole observed with sunrise/imax. *The Astrophysical Journal* **745**, 160 (2012).
- Hotta, H., Rempel, M., & Yokoyama, T. Efficient small-scale dynamo in the solar convection zone. *The Astrophysical Journal* **803**, 42 (2015).
- Huang, K.-Y., Chia, C.-M., & Chang, E. Optical resolution measurement system for small lens by using slanted-slit method. *Optical Measurement Systems for Industrial Inspection VIII*, SPIE, 705–712 (2013).
- Kosugi, T., Matsuzaki, K., Sakao, T., et al. The hinode (solar-b) mission: An overview. *Solar Physics* **1**, 3 (2007).
- Lites, B., Elmore, D., & Streander, K. The solar-b spectro-polarimeter. *Advanced solar polarimetry—theory, observation, and instrumentation*, 33 (2001).
- Lites, B. W. Rotating waveplates as polarization modulators for stokes polarimetry of the sun: evaluation of seeing-induced crosstalk errors. *Applied Optics* **26**, 3838 (1987).
- Martínez Pillet, V., Collados, M., Sánchez Almeida, J., et al. Lpsp & tip: full stokes polarimeters for the canary islands observatories. *High Resolution Solar Physics: Theory, Observations, and Techniques*, 264 (1999).
- Müller, D., Cyr, O. S., Zouganelis, I., et al. The solar orbiter mission-science overview. *Astronomy & Astrophysics* **642**, A1 (2020).
- Orozco Suárez, D., Álvarez García, D., López Jiménez, A. C., et al. Spgcam: A specifically tailored camera for solar observations. *Frontiers in Astronomy and Space Sciences* **10**, 1167540 (2023).
- Parker, E. Magnetic neutral sheets in evolving fields-part two-formation of the solar corona. *Astrophysical Journal*, Vol. 264, P. 642, 1983 **264**, 642 (1983).
- Petrovay, K., & Szakaly, G. The origin of intranetwork fields: a small-scale solar dynamo. *Astronomy and Astrophysics*, Vol. 274, p. 543 (1993) **274**, 543 (1993).
- Pillet, V. M., Bonet, J. A., Collados, M. V., et al. The imaging magnetograph experiment for the sunrise balloon antarctica project. *Optical, Infrared, and Millimeter Space Telescopes*, SPIE, 1152–1164 (2004).
- Pontin, D. I., & Hornig, G. The parker problem: existence of smooth force-free fields and coronal heating. *Living Reviews in Solar Physics* **17**, 5 (2020).
- Rempel, M., Bhatia, T., Bellot Rubio, L., & Korpi-Lagg, M. J. Small-scale dynamos: from idealized models to solar and stellar applications. *Space Science Reviews* **219**, 36 (2023).

- Sánchez, A., Gonzalo, A., Garranzo, D., et al. High precision and thermally controlled filter wheel. *Advances in Optical and Mechanical Technologies for Telescopes and Instrumentation V*, SPIE, 1120–1135 (2022).
- Scharmer, G. Comments on the optimization of high resolution fabry-pérot filtergraphs. *Astronomy & Astrophysics* **447**, 1111 (2006).
- Shibata, K., Nakamura, T., Matsumoto, T., et al. Chromospheric anemone jets as evidence of ubiquitous reconnection. *Science* **318**, 1591 (2007).
- Solanki, S. K., del Toro Iniesta, J., Woch, J., et al. The polarimetric and helioseismic imager on solar orbiter. *Astronomy & Astrophysics* **642**, A11 (2020).
- Tsuneta, S., Ichimoto, K., Katsukawa, Y., et al. The solar optical telescope for the hinode mission: an overview. *Solar Physics* **249**, 167 (2008).
- Van Noort, M., & van der Voort, L. R. Stokes imaging polarimetry using image restoration at the swedish 1-m solar telescope. *Astronomy & Astrophysics* **489**, 429 (2008).
- Vargas Dominguez, S. Study of horizontal flows in solar active regions based on high-resolution image reconstruction techniques. *Ph. D. Thesis* (2009).
- Wedemeyer-Böhm, S., Scullion, E., Steiner, O., et al. Magnetic tornadoes as energy channels into the solar corona. *Nature* **486**, 505 (2012).
- Zwaan, C. Elements and patterns in the solar magnetic field. IN: *Annual review of astronomy and astrophysics. Volume 25 (A88-13240 03-90)*. Palo Alto, CA, Annual Reviews, Inc., 1987, p. 83-111. **25**, 83 (1987).



1 one inch + \hoffset	2 one inch + \voffset
3 \oddsidemargin = -1pt	4 \topmargin = -7pt
5 \headheight = 14pt	6 \headsep = 19pt
7 \textheight = 631pt	8 \textwidth = 441pt
9 \marginparsep = 7pt	10 \marginparwidth = 88pt
11 \footskip = 30pt	\marginparpush = 7pt (not shown)
\hoffset = 0pt	\voffset = 0pt
\paperwidth = 597pt	\paperheight = 845pt



1 one inch + \hoffset	2 one inch + \voffset
3 \evensidemargin = 13pt	4 \topmargin = -7pt
5 \headheight = 14pt	6 \headsep = 19pt
7 \textheight = 631pt	8 \textwidth = 441pt
9 \marginparsep = 7pt	10 \marginparwidth = 88pt
11 \footskip = 30pt	\marginparpush = 7pt (not shown)
\hoffset = 0pt	\voffset = 0pt
\paperwidth = 597pt	\paperheight = 845pt